Corrosion Science 214 (2023) 111021

Contents lists available at ScienceDirect

Corrosion Science

journal homepage: www.elsevier.com/locate/corsci

# Corrosion behavior and protective performance of robustness mineralized layer formed on AZ80-0.38Nd (wt%) alloy

Chunlong Cheng [a,*], Zheng Chen [a], Yu Fan [a], Ruidong Yao [a], Qichi Le [b]

[a] School of Materials Science and Physics, China University of Mining and Technology, Xuzhou, Jiangsu 221116, People's Republic of China
[b] Key Laboratory of Electromagnetic Processing of Materials, Ministry of Education, Northeastern University, Shenyang 110819, People's Republic of China

ARTICLE INFO

*Keywords:*
Magnesium alloys
Surface treatment
Mineralized layer
Corrosion behavior
Protective performance

ABSTRACT

In our previous work, a novel robustness mineralized layer was prepared on surface of AZ80–0.38Nd (wt%) alloy, which mainly consisted of rod-like structure $MgCO_3$•3 $H_2O$ and flake structure 4$MgCO_3$•$Mg(OH)_2$•4 $H_2O$. The mineralized layer exhibited outstanding robustness structure. While its corrosion protection for magnesium alloy has not been explored. In this paper, the corrosion behavior and protective performance of the robustness mineralized layer were investigated via hydrogen evolution and electrochemical measurements, systematically. The results show that the mineralized layer exhibited excellent anti-corrosion property in the NaCl solution compared with the oxide layer, due to the outstanding impermeability. And the mineralized layer presented better corrosion passivation and micro-galvanic corrosion inhibition effects due to the characteristics of slight defects and good adhesion to matrix. Besides, the mineralized layer could launch $CO_3^{2-}$ during degradation of corrosion, which slowed down the penetration of $Cl^-$ across the layer and inhibited the attack of $Cl^-$ on magnesium substrate. The fabrication of robustness mineralized layer on magnesium alloys surface provides a novel effective strategy for improving the corrosion resistance of magnesium alloys.

## 1. Introduction

Magnesium alloy with a density of about 1.8 g/cm$^3$ is lighter than other structural alloys. And magnesium alloy is widely used in industrial circle, such as aerospace [1,2], computer [3], communication [4], consumer electronic [5], automobile [6], and health care industries [7], owing to the characteristics of light weight, excellent thermal and electrical conductivity, and good damping capacity. While the practical application of magnesium alloy is limited by its high chemical reactivity and poor corrosion resistance characteristics [3–5]. It suffers serious erosion in weak acidic aqueous solutions, even in neutral or weak alkaline aqueous solutions, so surface treatment is necessary for service life improvement of magnesium alloy in commercial and practical engineering application. The main surface treatment techniques for external protection of magnesium alloy include thermal spray coating [8], chemical coating [9], layered double hydroxide (LDH) coating [10,11], ion implantation [12], and plasma electrolytic oxidation (PEO) [13,14]. These technologies have played a certain role in magnesium alloy protection, but they still show irreparable disadvantages.

Recently, PEO technology has become a hot spot in surface treatment research of magnesium alloy [13–16]. PEO films show perfect effect on improving surface properties of magnesium alloy especially the corrosion resistance. Because in this process, high-energy discharges could melt magnesium alloy substrate, while the electrolyte could cool the molten oxide metal to form a ceramic film on alloy surface [15]. However, the huge operating voltages result in significant energy expense and a burden on the cost, which limited its rapid development and large-scale application. Besides, many other factors including the electrolyte concentration and composition, the electrolytic mode and current density, the type of substrates and the temperature and time of the coating process affect the plasma electrolytic oxidation process and energy consumption, that make the investigation more challenging [16].

LDH coatings have effective corrosion protection on magnesium alloy owing to the unique characteristics, such as structure memory effect, anion capacity, anion exchangeability, and barrier resistance [17]. As $A^{n-}$ ($CO_3^{2-}$, $NO_3^-$) were contained in LDH coating, corrosive anions (especially $Cl^-$) in the corrosion medium were exchanged by them, which can improve the corrosion resistance of magnesium alloy substrate and slow down the penetration of anions [10]. But the LDH films are thin and cannot absolutely cover the magnesium alloy substrate with the unavoidable porosity defects. And the stability of LDH film maybe is humble and will be lost in the acidic solution or high temperature

* Corresponding author.
*E-mail address:* iolxvxloi@163.com (C. Cheng).

https://doi.org/10.1016/j.corsci.2023.111021
Received 1 December 2022; Received in revised form 17 January 2023; Accepted 1 February 2023
Available online 7 February 2023

environment, which hampers the application range of LDH coating [11, 18]. Usually, other coatings are combined with LDH coating in order to improvement the corrosion resistance, which undoubtedly increases the complexity and cost of the process [19].

Some other surface treatment techniques for magnesium alloy are also widely used, such us thermal spray coating, chemical conversion coating, and ion implantation technology. However, they might show characteristics of environment unfriendly or poor impact and weather fastness that cannot provide corrosion protection for a long time. Thus, new effective surface treatment technologies need to develop and promote the large-scale application of magnesium alloy. In our previous work [20], a new surface treatment technology for magnesium alloy was proposed, i.e., surface treatment technology based on synergistic modification of oxidation and mineralization. And a novel robustness mineralized layer was prepared on surface of AZ80–0.38Nd (wt%) alloy, which mainly consisted of $MgCO_3$•3 $H_2O$ and $4MgCO_3$•$Mg(OH)_2$•4 $H_2O$. The mineralized layer exhibited outstanding robustness. But its corrosion protection for magnesium alloy has not been explored.

In this paper, the corrosion resistance of robustness mineralized layer on AZ80–0.38Nd alloy was investigated via hydrogen evolution and electrochemical measurements systematically, aiming to research the corrosion protection of the layer. Besides, the potential anti-corrosion mechanism was also discussed. Finally, the research provides a novel effective strategy for enhancing the anti-corrosion of magnesium alloys.

## 2. Experimental methods

### 2.1. Materials

The as-cast AZ80–0.38Nd alloy was used in this paper. The chemical composition of the alloy was evaluated using Inductively Coupled Plasma (ICP) emission spectroscopy and the values are displayed in Table 1. The testing samples used in this research were named as S0 (AZ80–0.38Nd alloy without surface treatment), S1 (AZ80–0.38Nd alloy with oxidization treatment, i.e., sample was oxidized with air flow at 420 °C for 4 h.) and S2 (AZ80–0.38Nd alloy with mineralization treatment, i.e., sample was oxidized with air flow at 420 °C for 4 h, then mineralized with water vapor and $CO_2$ flow at 40 °C for 10 h and pyrolyzed at temperature of 95 °C for 10 h.), which were listed in Table 2. And further details of surface treatment process of S0, S1 and S2 were provided in our previous work [20]. It should be noted that the AZ80–0.38Nd alloy was homogenized at 420 °C for 4 h before surface treatment to eliminate the impact of microstructure change on corrosion resistance.

### 2.2. Hydrogen evolution and electrochemical tests

In this research, hydrogen evolution was conducted for corrosion rate measurement. Samples (10 mm × 10 mm × 5 mm) for $H_2$ evolution test were sliced from treated specimens and cold mounted in epoxy resin of good adhesion, exposing an area of 10 × 10 $mm^2$ as shown in Fig. 1. As the cold mounted process was carefully and normatively conducted, there is no crevice between the mount and the metal sample, which prevents the initiation of crevice corrosion and ensures the accuracy of the experimental results. As for hydrogen collection, the sample was hung with a nylon string in a beaker with 500 ml 3.5 wt% NaCl solution for 246 h under an inverted glass funnel, and a 25 ml acid burette was employed to stockpile the hydrogen gas. The schematic diagram for hydrogen collection was illustrated in Fig. 2. And with the hydrogen volume got to the max capacities of the burette, 3.5 wt% sodium chloride solution was added in the burette. Then, the collected hydrogen was added up. The mixed solution comprised of a 200 g/L $CrO_3$, 10 g/L $AgNO_3$, and 20 g/L $BaNO_3$ was used to remove the corrosion products, according to ISO 8407 Standard [21]. The preparation of corrosive solution for immersion was reported in our previous works [22]. The average of three samples experimental results was adapted as the final result to ensure the reliability of testing data.

**Table 1**
Actual chemical compositions of AZ80–0.38Nd alloy.

| Elements | Al | Zn | Mn | Nd | Others | Mg |
|---|---|---|---|---|---|---|
| wt% | 7.98 | 0.55 | 0.33 | 0.38 | ≤0.10 | Balance |

**Table 2**
Samples for testing.

| Name | S0 | S1 | S2 |
|---|---|---|---|
| Process | Without surface treatment | Oxidization | Oxidization & Mineralization |

*The details of surface treatment process shown in our previous work [20].

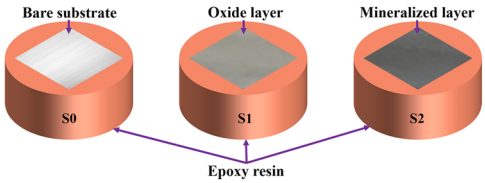


**Fig. 1.** Samples for hydrogen evolution and electrochemical tests.

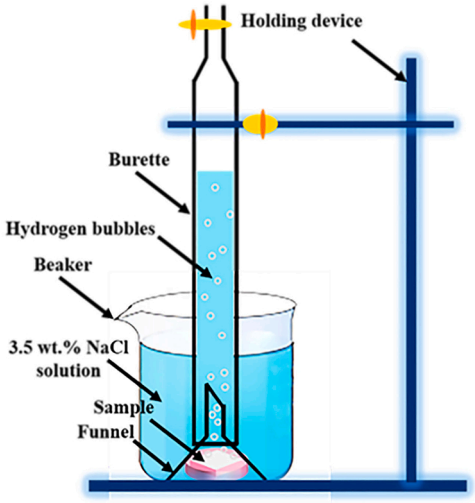


**Fig. 2.** The schematic diagram of hydrogen evolution experiments.

The electrochemical tests consisted of open circuit potential (OCP) measurement, electrochemical impedance spectroscopy (EIS) measurement and polarization curve measurement. The electrochemical tests were also performed in 3.5 wt% NaCl solution at 25 °C via employing an electrochemical workstation named ChenHua CHI660E. During the tests, the typical three-electrode system was hired, composed of the test sample as the working electrode (exposed surface immersed in the 3.5 wt% NaCl solution), a saturated calomel electrode (SCE, saturated KCl) as the reference electrode and a platinum foil as the counter electrode. For purpose of getting a possibly stable potential, the OCP test was performed for 3600 s. After that EIS measurement was conducted in $10^5$ Hz to $10^{-2}$ Hz with 5 mV alternating current amplitude signal at the OCP. Subsequently, the polarization curve was recorded with a scan rate of 1 $mVs^{-1}$ from − 2.1 $V_{SCE}$ to − 1.1 $V_{SCE}$. ZSimpWin Echem software was used for data fitting and analyzing. Additionally, three replicated samples were adapted. For electrochemical tests, the copper wire was attached to the rear part of the metal prior to mounting to ensure electrical connection.

### 2.3. Microstructures and surface morphologies identification

The surface morphologies of homogenized, oxidized and mineralized samples were observed by scanning electron microscope (SEM, FEI Quanta 450FEG). And a transmission electron microscopy (TEM, JEM-2100 F) is employed for second phase identify. In order to investigate the distinction of corrosion behaviors, the corrosion morphologies (removed corrosion products) of the samples were observed by the SEM. In addition, the cross-sectional morphologies of samples after corrosion were also analyzed by the SEM. And a SONY ILCE-A7M4 digital camera was employed to observe macroscopic morphologies of corroded samples.

## 3. Results and discussion

### 3.1. Microstructure and phase composition characterization

Fig. 3 shows the SEM microstructure with second phase EDS point analysis of S0, and surface morphologies of S1 and S2. Only needle-like $Al_2Nd$ phase appeared in AZ80–0.38Nd alloy matrix as shown in Fig. 3 (a,b). Usually, β-$Mg_{17}Al_{12}$ intermetallic particle would generate in AZ series alloy as Al concentrations above approximately 3 wt% [3]. The disappear of β-$Mg_{17}Al_{12}$ phase in this research was because the alloy had been homogenized at 420 °C for 4 h and β-$Mg_{17}Al_{12}$ phase were dissolved into the matrix. The similarly results were also reported in our previous work [23]. Besides, the TEM dark field images and selected

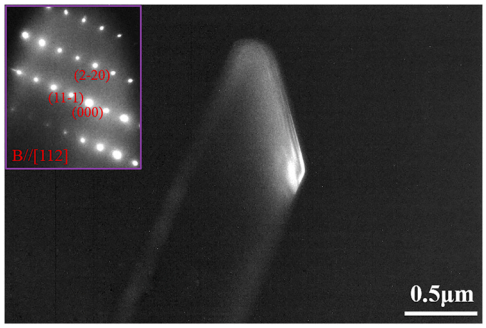


**Fig. 4.** TEM dark field image and selected area electron diffraction (SAED) pattern of $Al_2Nd$.

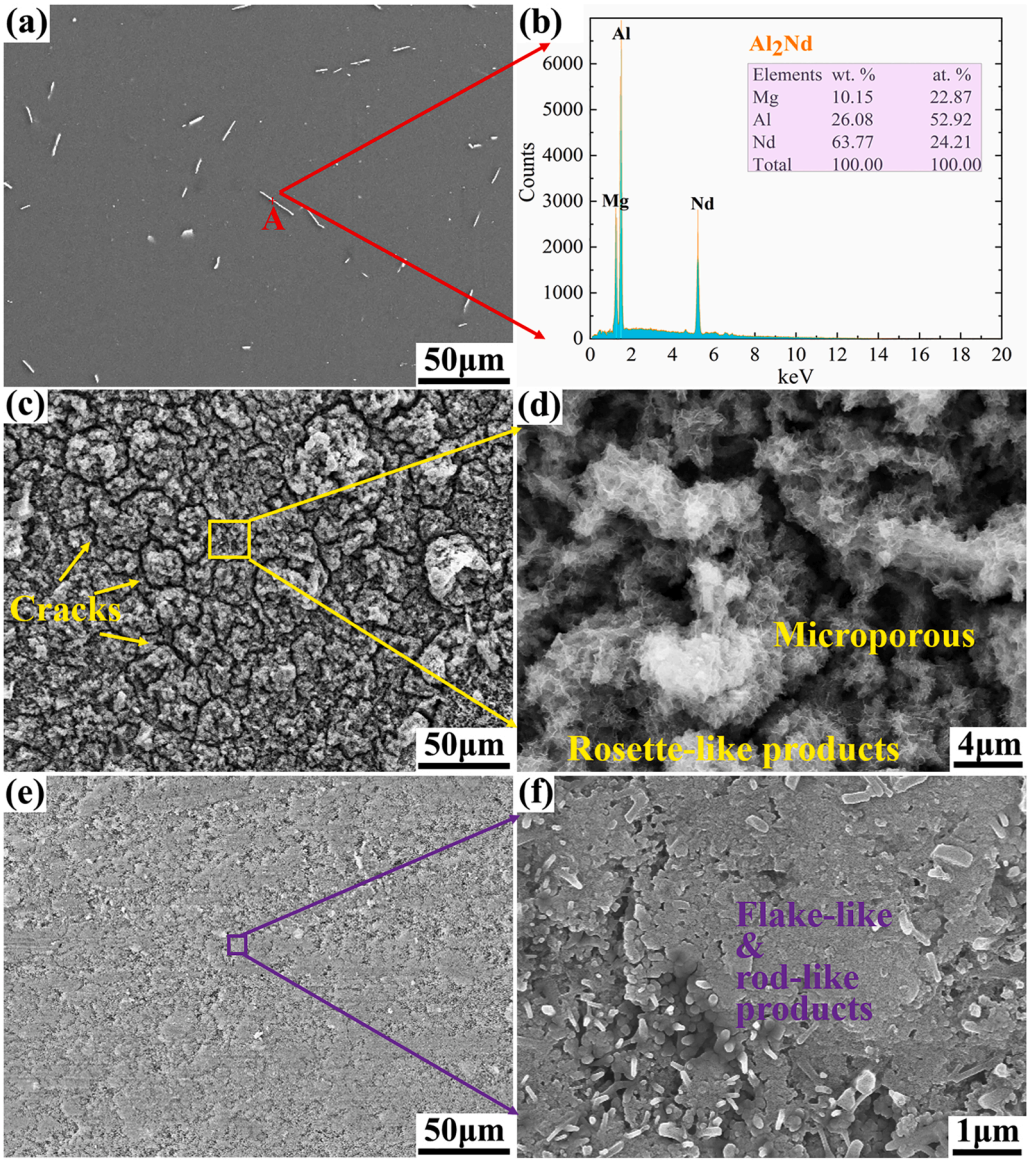


**Fig. 3.** SEM microstructure (a) with second phase EDS point analysis (b) of S0, and surface morphologies of S1 (c, d) and S2 (e, f).

area electron diffraction (SAED) patterns of $Al_2Nd$ were showed in Fig. 4, which also proved that $Al_2Nd$ was the only second phase of experimental alloys. One thing is certain, microstructure has an impact on the corrosion resistant of metallic materials including magnesium alloys [3]. Thus, the different corrosion resistance of S0, S1 and S2 is not primarily resulted by the microstructure in this research. Fig. 3(c,d) and (e,f) displays the surface morphologies of S1 and S2, respectively. It is clearly that the morphology and structure of oxide and mineralized layer show huge difference. The oxide layer fabricated on S1 surface was rough with cracks and big oxide nodules uneven distributed, while the mineralized layer propagated on S2 surface showed smooth and compact characteristics. In addition, the oxide products on S1 surface display rosette-like morphology (Fig. 3d). While surface of S2 was filled with flake-like and rod-like structure products (Fig. 3f).

Fig. 5 displays the SEM cross-sectional morphologies of S1 and S2 surface layers, which show more detail information about the oxide and mineralized layers. There are many oblique cracks in S1 surface layer, which across the oxide layer as shown in Fig. 5(a). This is consistent with the results in Fig. 3(c). Research reported that the origin of crack was driven by the association of the growth of the thermally grown oxide and the thermal mismatch between the substrate and the oxide layer, as the Pilling-Bedworth ratio of MgO is 0.81 [24,25]. Generally, during oxidation process, $Mg^{2+}$ ions diffused outward. In the same time, vacancies diffused inward, generating voids. After that the internal tensile stress, induced by the thicker oxide layer, cracked the oxide material already weakened by the voids. Stress could lead to cracking of the oxide layer and cracks extension in the oxide layer could result in releasing of residual stress [26]. While the mineralized layer exhibited bilayer structure as shown in Fig. 5(b). The outer layer displayed even and compact morphology, and the inner layer was with cracks but the cracking showed healing phenomenon compared with Fig. 5(a).

In addition, in our previous work, it is reported that the oxide layer (S1) mainly consisted of magnesium oxide and the mineralized layer (S2) was mainly composed of $MgCO_3{\bullet}3\,H_2O$ and $4MgCO_3{\bullet}Mg(OH)_2{\bullet}4\,H_2O$. MgO products presented porous structure. $MgCO_3{\bullet}3\,H_2O$ products showed rod-like crystal structure, while $4MgCO_3{\bullet}Mg(OH)_2{\bullet}4\,H_2O$ products displayed flake-like structure [20]. Thus, it is speculated that the differences in structure and composition between the oxide and mineralized layers would lead to differentiation of corrosion resistance.

### 3.2. Corrosion behaviors

Fig. 6 illuminated the hydrogen evolution curves of S0, S1 and S2 with the immersed time extension. Even though samples all exhibited an increase in the volume of hydrogen with the whole time of immersion, remarkable differentiation could be observed in the corrosion behavior, which reflected the significant difference of corrosion resistance. Fig. 6 (a) showed that two corrosion stages containing the incubation period of corrosion and accelerated corrosion were included of all samples as the corrosion process advanced. The incubation period of corrosion corresponds to quite low corrosion rates. And the incubation periods of S0, S1 and S2 were 8 h, 30 h and 78 h, respectively, as shown in Fig. 6(b). Besides, after 246 h immersion, the total hydrogen evolution volumes of S0, S1 and S2 were 19.42 ml/cm$^2$, 54.30 ml/cm$^2$ and 6.42 ml/cm$^2$, respectively. In addition, as the incubation period of corrosion and the total $H_2$ evolution volume of S1 was 30 h and 54.30 ml/cm$^2$, the oxide layer showed corrosion protective performance in the initial period of immersion. Subsequently, corrosion of S1 achieved higher rate owing to the defects of oxide layer and less protective products film. The corrosion preferentially started and grew at the defect sites, such as the cracks and holes as shown in Fig. 3(c,d). The result in Fig. 6(b) indicated that the oxide layer could provide 96 h protectiveness for magnesium substrate. Similar results were also reported in our other work [22]. And based on the above results and discussion, it can be concluded that S2 showed the best corrosion resistance which means the best corrosion protective performance of the mineralized layer.

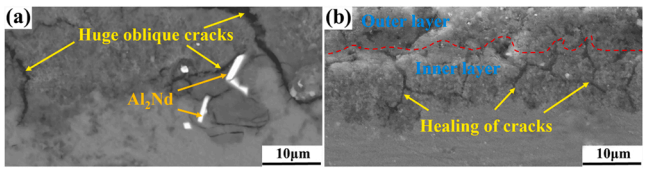


**Fig. 5.** The cross-sectional morphologies of S1 (a) and S2 (b) surface layers.

Fig. 7 exhibits the evolution of the OCP for samples in 3.5 wt% NaCl solution during 1 h of immersion. The three samples showed quite different behaviors, with the OCP drifting to more positive or negative values as immersed time elevated. The OCP of S0 drifted to more positive values with the extension of immersed time. This increase was obvious within the first 1000 s of testing. Then, the OCP tended to be stable. It is obviously that S1 displayed higher OCP values than S0 for all the time, but the OCP of S1 drifted to more negative values as immersed time extension, which was in direct contradiction to that of S0. This decrease was obvious within the first 1250 s of testing. Then the OCP tended to be stable. S2 showed the most special OCP behavior compared with S0 and S1. The OCP of S2 drifted to more negative values within the first 250 s, then to more positive values within 1250 s, after that the OCP tended to be stable. It should be noted that S2 exhibited the highest OCP values for all the time among the three. The more positive OCP values of magnesium alloy could be associated with a more noble behavior, thus with a higher corrosion resistance [27]. Accordingly, S2 demonstrated the noblest behavior and the highest corrosion resistance.

Report revealed that a drifted OCP value depicted the beginning and extension of corrosion, nevertheless a relatively stable OCP value indicated a stable state between the deposition of corrosion products and the advance of corrosion [28]. Thus, the OCP profiles suggest that at the initial period of immersion in 3.5 wt% NaCl solution, a relatively stable corrosion film formed on samples surface, which shifted the corrosion potential (OCP) in the noble direction. On the contrary, the slightly dissolution and immediate destruction of oxide, mineralized or corrosion product films in the $Cl^-$ contained solution resulted in shifting of corrosion potential (OCP) in the humble direction. The result showed in Fig. 7 indicated that dissolution and rupture of the mineralized layer might occur at the initial period of corrosion, while the corrosion products could repair the dissolution and rupture of the mineralized layer and corrosion passivation formed, meaning formation of a substantial uniform corrosion resistance film. Hence, S2 showed the best corrosion resistance.

Fig. 8 demonstrates the potentiodynamic polarization curves of S0, S1 and S2 with different immersed times. The results exhibited that S0, S1 and S2 showed similar cathodic polarization behaviors. All cathodic branches show particularly evident linear Tafel characteristic at potentials more negative than the critical potential, during which the main reaction is hydrogen evolution in aqueous solution [29]. The right branch of the polarization curve displays the anodic polarization, during which the primary behavior is dissolution of magnesium and abnormal anodic hydrogen evolution called negative difference effect (NDE), so the anodic polarization curve is too complicated to calculate corrosion current density and anodic branches could not be used for Tafel extrapolation [30]. The method of cathodic Tafel extrapolation was applied to estimate the corrosion current density ($i_{corr}$) of the potentiodynamic polarization curve. The junction of corrosion potential ($E_{corr}$) with cathodic Tafel slope had been used to calculate $i_{corr}$. The $E_{corr}$ and $i_{corr}$ results of S0, S1 and S2 for 1 h and 120 h immersion were listed in Table 3. The results indicated that S2 exhibited the smallest corrosion tendency and the lowest corrosion rate during the testing time, which also means the excellent protective performance for magnesium substrate of the mineralized layer. And the immense growth of $i_{corr}$ of S1 after 120 h immersion indicated the poor corrosion protection of the oxide layer. The results are consistent with the hydrogen evolution and

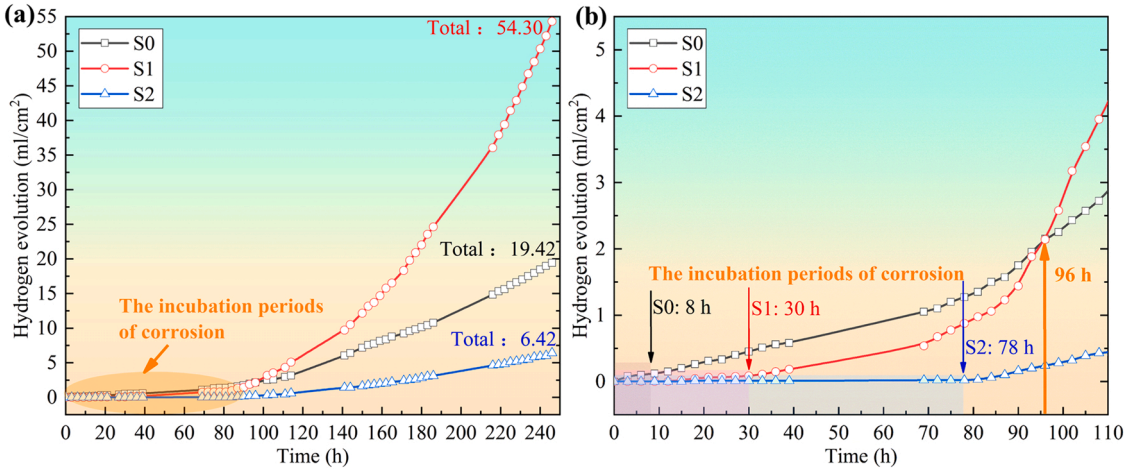


**Fig. 6.** Hydrogen evolution curves of test samples immersed in 3.5 wt% NaCl solution: (a) 0–246 h and (b) 0–110 h.

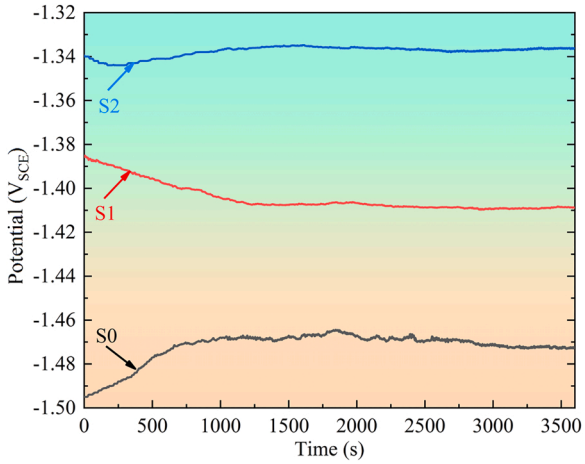


**Fig. 7.** Evolution of the OCP for S0, S1 and S2 samples in 3.5 wt% NaCl solution during 1 h of immersion.

OCP results. What is more, breakdown potential $E_b$ appeared in polarization curve of S2 no mater immersion for 1 h or 120 h. For immersed 1 h, $E_b$ was − 1.208 $V_{SCE}$, which was 111 mV higher than the $E_{corr}$. For immersed 120 h, $E_b$ was − 1.299 $V_{SCE}$, which was 91 mV higher than the $E_{corr}$. The results indicated that the mineralized layer exhibited effective corrosion protective performance, and passivation film formed during the corrosion process showed good stability and diffusion restrain effect of corrosive media $Cl^-$ [5,31]. In addition, after 120 h immersion, the corrosion current densities of S0, S1 and S2 all increased, which means the destruction of the oxide and mineralized layers. However, the mineralized layer still showed protective effect on magnesium substrate. Because passivation was not observed for S0 and S1 polarization curves, which indicated that the corrosion products did not show protective performance.

EIS tests were carried out to investigated the corrosion kinetic behaviors of S0, S1 and S2. Fig. 9 exhibits the EIS diagrams of samples after 1 h immersion in 3.5 wt% NaCl solution. The Nyquist diagrams of S0 and S1 consisted of two loops, i.e., one high frequency capacitance loop and one low frequency inductance loop. The two Nyquist diagrams were similar with the exception of the difference in the diameter of the loops. However, the Nyquist diagram of S2 only consisted of one capacitance

**Table 3**
$E_{corr}$ and $i_{corr}$ values of samples after immersed in 3.5 wt% NaCl solution for 1 h and 120 h.

| Samples | $E_{corr}$ (V vs. SCE) | | $\Delta E$ (V) | $i_{corr}$ (A/cm²) | | $\Delta i$ (A/cm²) |
|---|---|---|---|---|---|---|
| | 1 h | 120 h | | 1 h | 120 h | |
| S0 | -1.465 | -1.500 | -0.035 | 1.171E-4 | 8.322E-4 | 7.151E-4 |
| S1 | -1.365 | -1.469 | -0.104 | 1.013E-5 | 9.771E-4 | 9.670E-4 |
| S2 | -1.319 | -1.390 | -0.071 | 6.795E-6 | 3.393E-5 | 2.714E-5 |

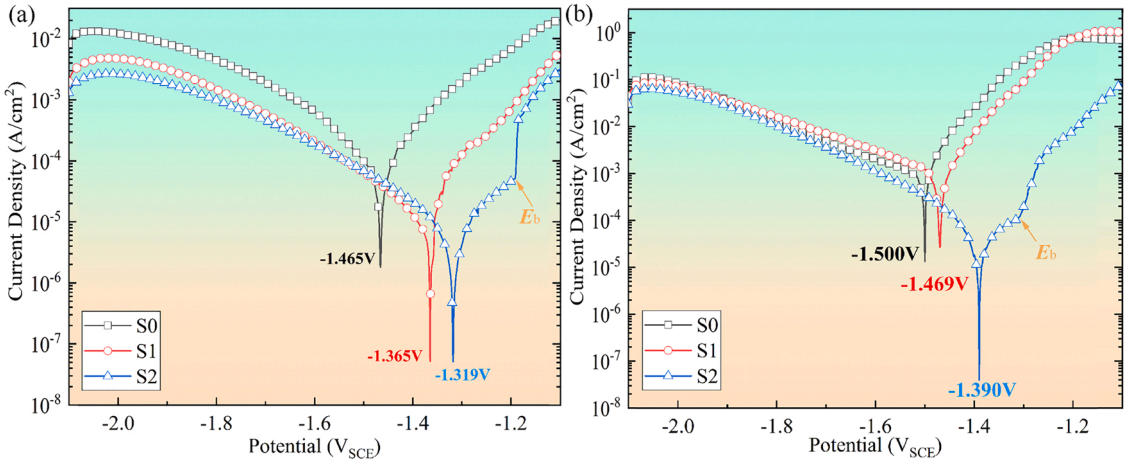


**Fig. 8.** Polarization curves of S0, S1 and S2 during immersion in 3.5 wt% NaCl solution for 1 h (a) and 120 h (b).

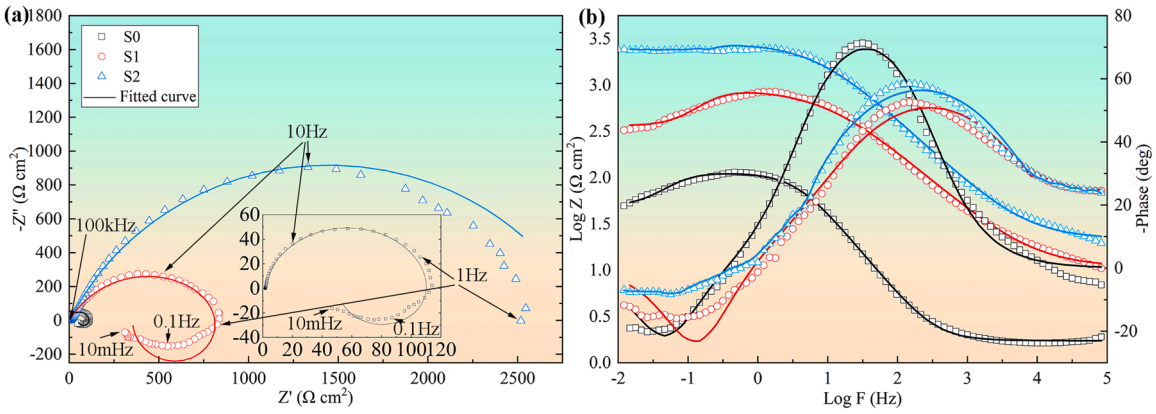


**Fig. 9.** EIS diagrams of samples after 1 h immersion in 3.5 wt% NaCl solution: (a) Nyquist plots and (b) Bode plots of impedance modulus and phase angle (vs. frequency).

loop at high frequency and the inductive loop disappeared. For 1 h immersion, the capacitance loop diameter could be ranked as S2 > S1 > S0. The capacitance loop diameter indicates the charge transfer process of $Mg/Mg^{2+}$ at the double layer formed at the surface film. Its diameter is equal to the charge transfer resistance of the working electrode [32]. And the induction loop is generally considered to be related to the pitting corrosion [33]. In addition, at the low frequency zone between $10^{-2}$ and 1 Hz, the samples impedance Z are clearly observed as shown in Fig. 9(b). The Z values could be ranked as S2 > S1 > S0, meaning that samples corrosion resistance might also follow this order. And the phase angles of the S2 with only one peak exhibit wider than the S0 and S1 at intermediate frequencies.

What is more, the Nyquist plots in Fig. 9 were fitted via ZSimpWin software. Three equivalent electrical circuits were obtained as depicted in Fig. 10. And the fitted EIS data presented in Fig. 10 were also acquired as listed in Table 4. To be sure, $R_s$ is the solution resistance. $CPE_{dl}$ and $R_t$ present the double layer capacitance and the charge transfer resistance, respectively. $R_x$ shows the layer resistance paralleled with constant phase element $CPE_x$. L and $R_L$ are inductance and inductive resistance, which demonstrate the low frequency inductive loop. $CPE_{dl}$ and $CPE_x$ supplant the ideal capacitors due to the system nonuniformity, such as electrode porosity, slow adsorption reactions and surface roughness [8, 18,34]. As shown in Table 4, the layer resistances of S1 and S2 are 892.20 and 2893.00 Ω·cm$^2$, respectively. The result means that the mineralized layer exhibits better charge transfer resistance, i.e., the mineralized layer is denser than the oxide layer. This result can also be proved by the $CPE_x$ of S1 and S2. In Table 4, the capacitance ($CPE_x$) of S2 is an order of magnitude lower than that of S1, which means lower coating defects of S2. And excellent coating structure of S2 suppressed the dissolution of the substrate and pitting corrosion, resulting disappear of low frequency inductance loop. Thus, it can be concluded that S2 provided the best corrosion resistance compared with S0 and S1, which means the best corrosion protective performance of the mineralized layer.

To evaluate the corrosion protection of the mineralized layer after 120 h immersion in 3.5 wt% NaCl solution, EIS tests were also carried out. The results were displayed in Fig. 11. The low frequency inductance loop appeared in Nyquist diagrams of S2, indicating the devastation of the mineralized layer and occurrence of pitting corrosion. Besides, the diameters of the capacitive loops of S0, S1 and S2 all decreased with prolonged immersion time, indicating the significantly degradation and destruction of the oxide and mineralized layers. Once the corrosion medium penetrated the oxide or mineralized layer through the defects and reached the substrate, corrosion occurred leading to a sharp drop in capacitive loop diameter [4]. While S2 still show the biggest capacitive loop diameter compared with S0 and S1, meaning the best corrosion resistance property.

In addition, Fig. 12 showed the equivalent electrical circuit of Nyquist plots in Fig. 11 fitted via ZSimpWin software. Table 5 presented the Fitted EIS data presented in Fig. 12. $R_L$ and L appeared in the equivalent electrical circuit of S2, corresponding to the low frequency inductance loop. And the results show that $R_x$, $R_L$ and L all could be ranked as S1 > S2 > S0. But $R_x$ of S2 was two orders of magnitude higher than that of S0 and S1. And the phase angles of S2 in Fig. 10 (b) also exhibited wider than the S0 and S1 at intermediate frequencies. The above results indicated that after 120 h immersion, S2 still exhibited the best corrosion resistance due to the corrosion protective performance of the mineralized layer.

### 3.3. Analysis of corrosion morphologies

Fig. 13 shows the corrosion macroscopic morphologies of S0, S1 and S2 after immersion in 3.5 wt% NaCl solution for different times. Before immersion, the surface of S0 shows metallic luster. While surfaces of S1 and S2 present grayish white and gray black structure, respectively, owing to covering of oxide or mineralized layers. After 24 h immersion, lots of white corrosion spots, composed mainly of magnesium hydroxide [5,22,28], grew and scattered on surfaces of S0 and S1. While almost no corrosion spots appeared on surface of S2, indicating the slightly corrosion degree with mineralized layer protection. And after 120 h

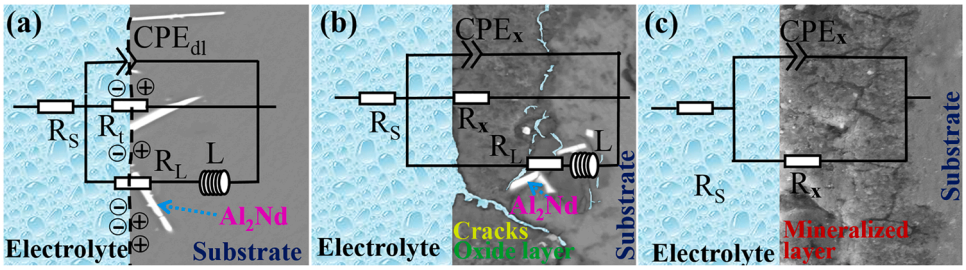


**Fig. 10.** Equivalent electrical circuits used for the simulation of EIS data in Fig. 9: (a) S0, (b) S1 and (c) S2.

**Table 4**
Fitted EIS data on basis of equivalent circuit presented in Fig. 10.

| Samples | $R_s$ Ω·cm² | $CPE_{dl}$ Ω⁻¹·cm⁻²·sⁿ | $n_{dl}$ | $R_t$ Ω·cm² | $CPE_x$ Ω⁻¹·cm⁻²·sⁿ | $n_x$ | $R_x$ Ω·cm² | $R_L$ Ω·cm² | L H·cm² |
|---|---|---|---|---|---|---|---|---|---|
| S0 | 7.27 | 4.90E-4 | 0.93 | 111.00 | – | – | – | 88.97 | 442.10 |
| S1 | 10.67 | – | – | – | 6.28E-5 | 0.68 | 892.20 | 587.50 | 1093.00 |
| S2 | 11.46 | – | – | – | 2.21E-6 | 0.72 | 2893.00 | – | – |

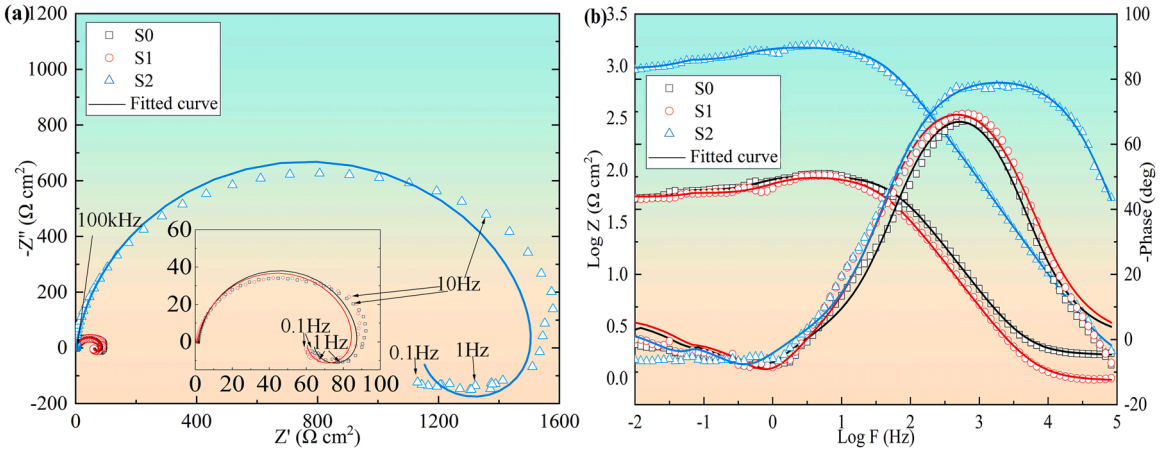


**Fig. 11.** Samples EIS diagrams after immersion in 3.5 wt% NaCl solution for 120 h: (a) Nyquist plots and (b) Bode plots of impedance modulus and phase angle (vs. frequency).

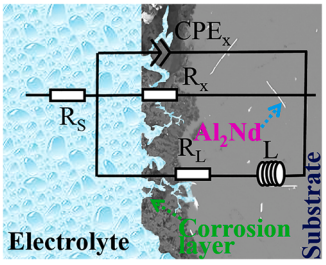


**Fig. 12.** Equivalent electrical circuits used for the simulation of EIS data in Fig. 11.

**Table 5**
Fitted EIS data on basis of equivalent circuit presented in Fig. 12.

| Samples | $R_s$ Ω·cm² | $CPE_x$ Ω⁻¹·cm⁻²·sⁿ | $n_x$ | $R_x$ Ω·cm² | $R_L$ Ω·cm² | $L$ H·cm² |
|---|---|---|---|---|---|---|
| S0 | 12.84 | 5.18E-4 | 0.91 | 87.26 | 218.10 | 68.67 |
| S1 | 9.55 | 8.41E-5 | 0.90 | 86.69 | 188.50 | 40.56 |
| S2 | 13.35 | 4.17E-6 | 0.91 | 1532.00 | 4493.00 | 1951.00 |

immersion, corrosion products on S0 and S1 surfaces increased and piled into nodular, due to the less protective products film. However, corrosion of S2 was inapparent with scattered pitting eclipses and peel-off areas. After 240 h immersion, a large number of snow-white corrosion products accumulated on the surfaces of S0 and S1, which were accompanied by large and deep corrosion holes. And S0 and S1 showed uneven corrosion characteristic. Though the corrosion of S2 was aggravated with time increasing, no corrosion hole appeared in the surface. And spallation of the mineralized layer occurred due to the boundary cracks and the mineralized layer bending and rupturing, or longitudinal cracks which do not run through the layer, which results from accumulation of corrosion products at the interface between mineralized layer and substrate [22,35,36]. Seen from the macroscopic morphology of corrosion, the evaluation corrosion degree of samples was ranked as S1 > S0 > S2, which was in line with the results of hydrogen evolution and EIS tests.

Fig. 14 displays S0, S1 and S2 microscopic corrosion morphologies without corrosion products after being immersed 240 h in 3.5 wt% NaCl solution. It is obvious that S0 and S1 showed localized corrosion characteristic, and the corroded areas form big and deep pits as shown in Fig. 14 (a,b). Exposed $Al_2Nd$ phase distributed in the corrosion pits. Electrochemical potential difference between second-phase particle and substrate is of importance associated with corrosion [36]. Besides, corrosion pits distributed mostly along the $Al_2Nd$ boundaries, which means α-Mg was dissolved during corrosion process, i.e., micro-galvanic couples generated between $Al_2Nd$ phases and α-Mg due to the electrochemical potential difference, and α-Mg acted as anode. Accordingly, $Al_2Nd$ was used as cathode that was protected. This is in line with the reports by Dargusch [37], Song [38] and Arrabal [39]. Uniform corrosion characteristic was present to the S2 as shown in Fig. 14 (c). Cracks and small corrosion sockets (about 5–15 μm) propagated on the mineralized layer. Thus, during the corrosion process, the peel-off area and cracks offer passways for corrosive ions penetration, and remarkably weaken the corrosion resistance performance of the robustness mineralized layer.

Fig. 15 gives the microscopic morphologies of the corrosion cross-sections of S0, S1 and S2 after being immersed 240 h, which emphasizes some detailed information about corrosion behaviors. Typical localized corrosion could be observed of S0 and S1 as shown in Fig. 15 (a,b) and (c,d), respectively. The corrosion lunched conveniently at sample surface, owing to the formation of micro-galvanic couples between α-Mg and $Al_2Nd$ particles. Then micro-galvanic corrosion expended to pitting. Finally, corrosion of S0 and S1 extended from surface to substrate, leaving huge pits and presenting localized corrosion characteristic. As S2 covered with dense and intact mineralized layer, micro-galvanic corrosion of S2 was inhibited during the corrosion process [22]. And there is no typical localized corrosion occurred even after 240 h immersion, owing to the dense structure, perfect hydrophobicity and good robustness of the mineralized layer. Because dense and intact coating shows excellent physical isolation and penetration inhibition of corrosive solution [4,13]. What is more, reports show that the $A^{n-}$

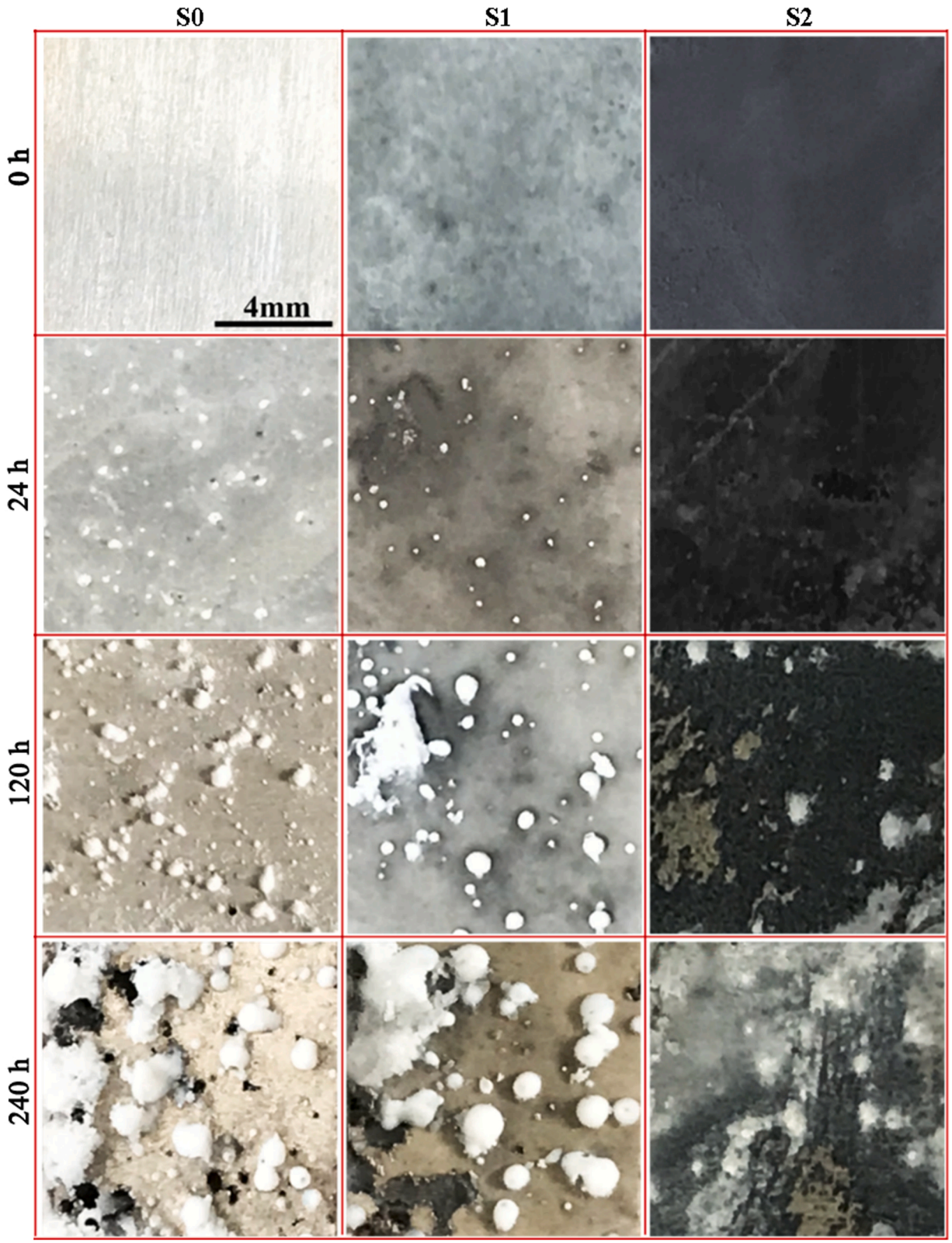


**Fig. 13.** Macroscopic corrosion morphologies of S0, S1 and S2 after being immersed for different times in 3.5 wt% NaCl solution.

($CO_3^{2-}$) could exchange with $Cl^-$, which would restrain anions penetration and enhance Mg alloy corrosion resistance [10,40]. The mineralized layer (S2) contained more magnesium carbonate salts compared with the oxide layer (S1) as reported in our previous work [20], which means the mineralized layer can undoubtedly provide more $CO_3^{2-}$ during degradation. And Zhang et al. reported that the presence of $CO_3^{2-}$ in the diffusion boundary layer impaired the adsorption of $Cl^-$ on the surface of the coating due to competitive adsorption [40]. Therefore, the diffusion boundary of the mineralized layer containing $CO_3^{2-}$ can effectively improve the pitting resistance property of the magnesium

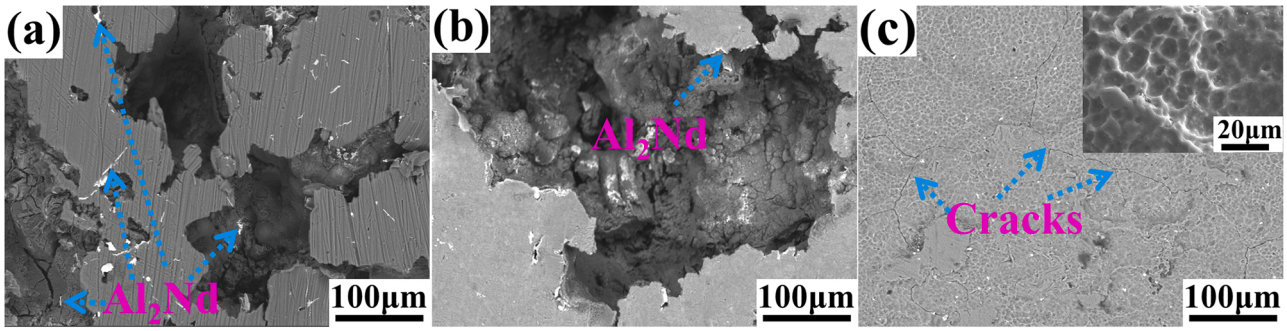


**Fig. 14.** Microscopic corrosion morphologies of S0 (a), S1 (b) and S2 (c) without corrosion products after being immersed 240 h in 3.5 wt% NaCl solution.

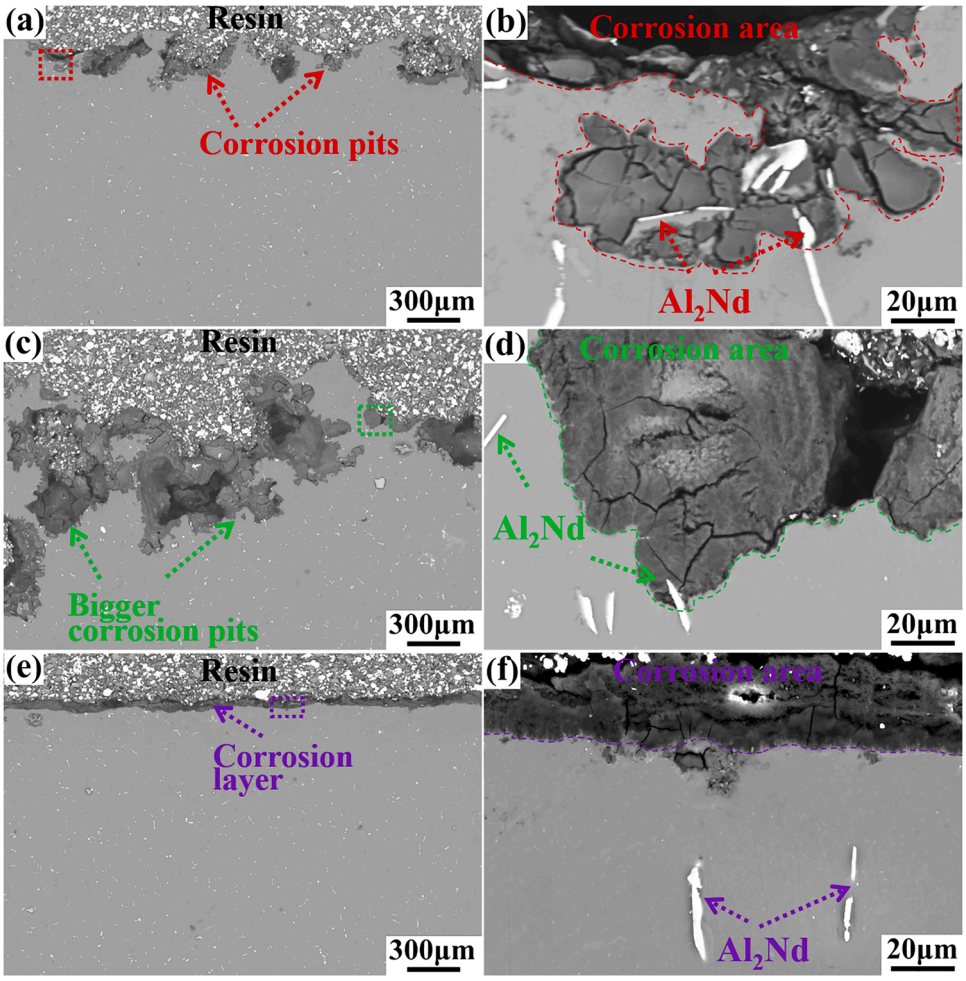


**Fig. 15.** Microscopic morphologies of the corrosion cross-sections of S0 (a,b), S1 (c,d) and S2 (e,f) after being immersed 240 h in 3.5 wt% NaCl solution.

alloy surface, as shown in Fig. 15. And based on the experimental results, a model is used to illustrate the mechanisms of competitive adsorption, as shown in Fig. 16. And the competitive adsorption between $CO_3^{2-}$ and $Cl^-$ hindered the $Cl^-$ adsorption on the mineralized layer surface, increasing the layer pitting resistance property. Thus, the localized corrosion of S2 was restrained, and corrosion of S2 spread evenly and slowly to the substrate layer by layer. Notionally, inhibiting direct electrical contact between magnesium alloy and corrosion medium can slow down corrosion [19]. Thus, the formation of a nice insulating film between the substrate and corrosion medium is beneficial to weaken corrosion damage. And the mineralized layer is an excellent corrosion protective layer due to its unique characteristics.

## 4. Conclusions

The main conclusions are summarized as:

(1) The mineralized layer with robustness structure and slight defects exhibited excellent anti-corrosion property in the NaCl solution compared with the defective oxide layer. And the outstanding combination of the mineralized layer and magnesium substrate greatly improved the corrosion resistance and impermeability of the mineralized layer.
(2) The mineralized layer presented better corrosion passivation and micro-galvanic corrosion inhibition characteristics due to the

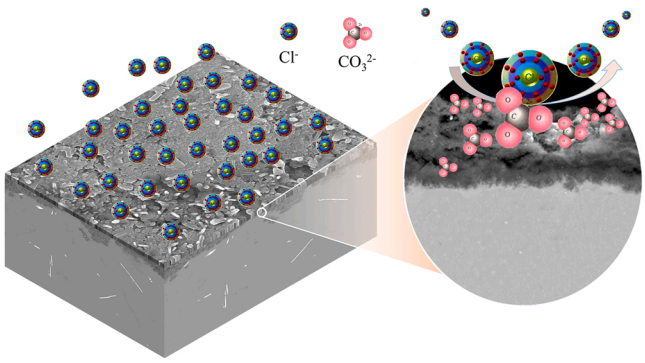


**Fig. 16.** The model of release $CO_3^{2-}$ and competitive adsorption between $CO_3^{2-}$ and $Cl^-$ of the mineralized layer during corrosion process.

characteristics of slight defects and good adhesion to matrix, which promoted corrosion of magnesium alloy to develop slowly and uniformly. Besides, the existence of defects in the mineralized layer makes it possible to further enhance the corrosion protective performance.

(3) The mineralized layer contained lots of magnesium carbonate salts could launch $CO_3^{2-}$ during degradation of corrosion, which slowed down the penetration of $Cl^-$ across the mineralized layer to the magnesium substrate and inhibited the attack of $Cl^-$ on magnesium substrate.

(4) The formation of robustness mineralized layer on magnesium alloys surface provides a novel effective strategy for increasing the corrosion resistance of magnesium alloys.

## CRediT authorship contribution statement

**Chunlong Cheng:** Conceptualization, Writing – original draft, Writing – review & editing. **Zheng Chen:** Methodology, Validation, Supervision. **Yu Fan:** Validation, Formal analysis, Visualization. **Ruidong Yao:** Supervision, Data curation. **Qichi Le:** Validation, Data curation.

## Declaration of Competing Interest

The authors declare that they have no known competing financial interests or personal relationships that could have appeared to influence the work reported in this paper.

## Data availability

The data that has been used is confidential.

## Acknowledgements

The authors thankfully acknowledge the Material Science and Engineering Discipline Guidance Fund of China University of Mining and Technology (CUMTMS202210), National Natural Science Foundation of China (Nos. 52274377 and 52274401). Special thanks are due to the instrumental or data analysis from Analytical and Testing Center, Northeastern University and China University of Mining and Technology.

## References

[1] F. Czerwinski, Controlling the ignition and flammability of magnesium for aerospace applications, Corros. Sci. 86 (2014) 1–16.
[2] Z. Hu, Q.X. Zhang, Casting technology and quality control of aluminum and magnesium alloy, Aerosp. Ind. Press (1990) 6–10.
[3] K. Gusieva, C.H.J. Davies, J.R. Scully, N. Birbilis, Corrosion of magnesium alloys: the role of alloying, Int. Mater. Rev. 60 (2015) 169–194.
[4] S. Feliu Jr., A. Samaniego, V. Barranco, A.A. El-Hadad, I. Llorente, C. Serra, J. C. Galván, A study on the relationships between corrosion properties and chemistry of thermally oxidised surface films formed on polished commercial magnesium alloys AZ31 and AZ61, Appl. Surf. Sci. 295 (2014) 219–230.
[5] Y. Ma, H. Xiong, B. Chen, Effect of heat treatment on microstructure and corrosion behavior of Mg-5Al-1Zn-1Sn magnesium alloy, Corros. Sci. 191 (2021), 109759.
[6] C. Dagger, MAG TECH 1: Magnesium Alloys and Processing Technologies for Lightweight Transport Applications-a Mission to Europe, Report of a DTI Global Watch Mission, September/October 2004, 25–31.
[7] Y. Li, Y. Wang, Z. Shen, F. Miao, J. Wang, Y. Sun, S. Zhu, Y. Zheng, S. Guan, A biodegradable magnesium alloy vascular stent structure: design, optimisation and evaluation, Acta Biomater. 142 (2022) 402–412.
[8] M. Carboneras, M.D. López, P. Rodrigo, M. Campo, B. Torres, E. Otero, J. Rams, Corrosion behaviour of thermally sprayed Al and Al/SiCp composite coatings on ZE41 magnesium alloy in chloride medium, Corros. Sci. 52 (2010) 761–768.
[9] P. Zhou, B. Yu, Y. Hou, G. Duan, L. Yang, B. Zhang, T. Zhang, F. Wang, Revisiting the cracking of chemical conversion coating on magnesium alloys, Corros. Sci. 178 (2021), 109069.
[10] L. Hou, Y. Li, J. Sun, S.H. Zhang, H. Wei, Y. Wei, Enhancement corrosion resistance of Mg Al layered double hydroxides films by anion-exchange mechanism on magnesium alloys, Appl. Surf. Sci. 487 (2019) 101–108.
[11] Z. Xie, L. Wu, Corrosion inhibition of layered double hydroxide coating for Mg alloy in acidic corrosive environments, Mater. Corros. 71 (2020) 118–124.
[12] F. Czerwinski, The reactive element effect on high-temperature oxidation of magnesium, Int. Mater. Rev. 60 (2015) 264–296.
[13] R.O. Hussein, D.O. Northwood, X. Nie, The influence of pulse timing and current mode on the microstructure and corrosion behaviour of a plasma electrolytic oxidation (PEO) coated AM60B magnesium alloy, J. Alloy. Compd. 541 (2012) 41–48.
[14] E. Matykina, R. Arrabal, M. Mohedano, B. Mingo, J. Gonzalez, A. Pardo, M. C. Merino, Recent advances in energy efficient PEO processing of aluminium alloys, Trans. Nonferrous Met. Soc. China 27 (2017) 1439–1454.
[15] E. Matykina, R. Arrabal, A. Pardo, M. Mohedano, B. Mingo, I. Rodríguez, J. González, Energy-efficient PEO process of aluminium alloys, Mater. Lett. 127 (2014) 13–16.
[16] H. Huang, X. Wei, J. Yang, J. Wang, Influence of surface micro grooving pretreatment on MAO process of aluminum alloy, Appl. Surf. Sci. 389 (2016) 1175–1181.
[17] Y. Cao, D. Zheng, F. Zhang, J. Pan, C. Lin, Layered double hydroxide (LDH) for multi-functionalized corrosion protection of metals: a review, J. Mater. Sci. Technol. 102 (2022) 232–263.
[18] Z. Song, Z. Xie, L. Ding, Y. Zhang, X. Hu, Preparation of corrosion-resistant MgAl-LDH/Ni composite coating on Mg alloy AZ31B, Colloids Surf. A 632 (2022), 127699.
[19] Y. Li, Y. Ouyang, R. Fang, X. Jiang, Z.-H. Xie, L. Wu, J. Long, C.-J. Zhong, A nickelunderlayer/LDH-midlayer/siloxane-toplayer composite coating for inhibiting galvanic corrosion between Ni layer and Mg alloy, Chem. Eng. J. 430 (2022), 132776.
[20] C. Cheng, Q. Le, C. Hu, T. Wang, Q. Liao, X. Li, Preparation of a novel robustness mineralized layer on surface of AZ80-0.38Nd (wt%) alloy and investigation of its properties, Appl. Surf. Sci. 600 (2022), 153970.
[21] ISO 8407 Standard , 2021 Corrosion of Metals and Alloys—Removal of Corrosion Products From Corrosion Test Specimens.
[22] C. Cheng, Q. Le, C. Hu, W. Hu, T. Wang, B. Zhu, X. Zhou, Understanding on corrosion mechanism of oxidized AZW800 alloy in 3.5 wt% NaCl solution, J. Magnes. Alloys xxx (xxx) xxx, https://doi.org/10.1016/j.jma.2021.08.015.
[23] C. Cheng, Q. Le, D. Li, W. Hu, T. Wang, R. Guo, C. Hu, Effect of Y on high-temperature oxidation behavior and products of AZ80 alloy, Mater. Chem. Phys. 269 (2021), 124732.
[24] Y. Chen, X. Zhao, M. Bai, L. Yang, C. Li, L. Wang, J.A. Carr, P. Xiao, A mechanistic understanding on rumpling of a NiCoCrAlY bond coat for thermal barrier coating applications, Acta Mater. 128 (2017) 31–42.
[25] Y.M. Kim, C.D. Yim, H.S. Kim, B.S. You, Key factor influence the ignition resistance of magnesium alloys at elevated temperatures, Scr. Mater. 65 (2011) 958–961.
[26] B.Q. Xu, L.R. Luo, J. Lu, X.F. Zhao, P. Xiao, Effect of residual stress on the spallation of the thermally-grown oxide formed on NiCoCrAlY coating, Surf. Coat. Technol. 381 (2020), 125112.
[27] R. Reyes-Riverol, M. Lieblich, S. Fajardo, Corrosion resistance and anomalous hydrogen evolution in chloride containing solutions of extruded cast and powder metallurgical Mg-1Zn alloy, Corros. Sci. 208 (2022), 110635.
[28] M.C. Zhao, M. Liu, G.L. Song, A. Atrens, Influence of pH and chloride ion concentration on the corrosion of Mg alloy ZE41, Corros. Sci. 50 (2008) 3168–3178.
[29] Y. Cubides, D. Zhao, L. Nash, D. Yadav, K. Xie, I. Karaman, H. Castaneda, Effects of dynamic recrystallization and strain-induced dynamic precipitation on the corrosion behavior of partially recrystallized Mg–9Al–1Zn alloys, J. Magnes. Alloy. 8 (2020) 1016–1037.
[30] Q. Liu, Q. Ma, G. Chen, X. Cao, S. Zhang, J. Pan, G. Zhang, Q. Shi, Enhanced corrosion resistance of AZ91 magnesium alloy through refinement and homogenization of surface microstructure by friction stir processing, Corros. Sci. 138 (2018) 284–296.
[31] R.Z. Xu, X.B. Yang, P.H. Li, K.W. Suen, S. Wu, P.K. Chu, Eelectrochemical properties and corrosion resistance of carbon-ion-implanted magnesium, Corros. Sci. 82 (2014) 173–179.

[32] Q. Liu, G.Q. Chen, S.B. Zeng, S. Zhang, F. Long, Q.Y. Shi, The corrosion behavior of Mg-9Al-xRE magnesium alloys modified by friction stir processing, J. Alloy. Compd. 851 (2021), 156835.
[33] S. Liu, Y. Qi, Z. Peng, J. Liang, A chemical-free sealing method for micro-arc oxidation coatings on AZ31 mg alloy, Surf. Coat. Technol. 406 (2021), 126655.
[34] M. Ascencio, M. Pekguleryuz, S. Omanovic, An investigation of the corrosion mechanisms of WE43 Mg alloy in a modified simulated body fluid solution: the effect of electrolyte renewal, Corros. Sci. 91 (2015) 297–310.
[35] L. Li, G. Swain, Effects of aging temperature and time on the corrosion protection provided by trivalent chromium process coatings on AA2024-T3, ACS Appl. Mater. Interfaces 5 (2013) 7923–7930.
[36] J.H.W. de Wit, Local potential measurements with the SKPFM on aluminium alloys, Electrochim. Acta 49 (2004) 2841–2850.
[37] M.S. Dargusch, G.L. Dunlop, K. Pettersen, in: B.L. Mordike, K.U. Kainer (Eds.), Magnesium Alloys and Their Applications, Werkstoff-informations GmbH, Wolfsburg, Germany, 1998, pp. 277–282.
[38] G.L. Song, Corrosion and Protection of Magnesium Alloy, Chemical Industry Press, 2006, pp. 169–170.
[39] R. Arrabal, B. Mingo, A. Pardo, E. Matykina, M. Mohedano, M.C. Merino, A. Rivas, A. Maroto, Role of alloyed Nd in the microstructure and atmospheric corrosion of as-cast magnesium alloy AZ91, Corros. Sci. 97 (2015) 38–48.
[40] F. Zhang, Z.-G. Liu, R.-C. Zeng, S.-Q. Li, H.-Z. Cui, L. Song, E.-H. Han, Corrosion resistance of Mg–Al-LDH coating on magnesium alloy AZ31, Surf. Coat. Technol. 258 (2014) 1152–1158.